Ecotoxicology and Environmental Safety 290 (2025) 117747

Contents lists available at ScienceDirect

Ecotoxicology and Environmental Safety

journal homepage: www.elsevier.com/locate/ecoenv

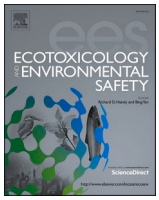

# Effects of pesticide dichlorvos on liver injury in rats and related toxicity mechanisms

Pengcheng Zhang [a,b,1], Zixian Zhou [c,1], Jiaqi Yao [a,1], Yuhong Jiang [a], Hang Lei [a], Zhijun Xie [d], Juan Li [a], Xianlin Zhao [a], Lv Zhu [a], Meihua Wan [a], Ling Liu [c], Wenfu Tang [a,b,*]

[a] West China Center of Excellence for Pancreatitis, Institute of Integrated Traditional Chinese and Western Medicine, West China Hospital, Sichuan University, Chengdu 610041, China
[b] Regenerative Medicine Research Center, Sichuan University West China Hospital, Chengdu, Sichuan 610041, China
[c] Department of Neurology, West China Hospital, Sichuan University, Chengdu 610041, China
[d] Department of Spleen and Stomach Diseases, The Affiliated Traditional Chinese Medicine Hospital of Southwest Medical University, Lu zhou, Sichuan 646000, China

ARTICLE INFO

Edited by: Professor Bing Yan

*Keywords:*
Dichlorvos
Liver damage
IRGM
Incomplete autophagy
Apoptosis
Ferroptosis

ABSTRACT

Dichlorvos (DDVP) is an organophosphorus pesticide commonly utilized in agricultural production. Recent epidemiological studies suggest that exposure to DDVP correlates with an increased incidence of liver disease. However, data regarding the hepatotoxicity of DDVP remain limited. Additionally, the regulatory mechanisms underlying DDVP-induced liver injury have not been thoroughly investigated. In this study, we utilized Wistar rats and BRL-3A cells to establish in vivo and in vitro models for examining the effects of DDVP exposure on liver damage. Our findings indicate that DDVP impairs hepatocyte autophagy and increases ROS activity. RNA sequencing and metabolomic analyses revealed that the pathways affected by DDVP exposure in hepatocytes include ABC transporters and amino acid biosynthesis processes. Furthermore, targeting IRGM overexpression through hepatic portal vein injection of adeno-associated virus mitigated DDVP-induced liver injury. These results demonstrate that DDVP exposure induces liver damage in rats through mechanisms that are dependent on ROS and autophagy, at least in part by downregulating IRGM. Our study offers new insights into the molecular mechanisms of liver injury following organophosphate poisoning and suggests that IRGM may represent a novel therapeutic target for DDVP-induced liver injury.

## 1. Introduction

Pesticides, including insecticides, herbicides, and fungicides, are chemical agents utilised in agricultural production (Ebel et al., 2021). According to statistics, over 5.6 billion pounds of pesticides are applied annually, providing substantial benefits to agricultural output (Brown et al., 2021). However, the intensive use of these chemicals has led to significant environmental impacts, particularly those as a result of their residues in ecosystems, including air, soil, and water sources (Megharaj et al., 2011). Pesticide pollution has emerged as a prevalent form of environmental contamination, posing serious threats to both human and animal health. In recent years, potential health risks linked to pesticide contamination have garnered considerable attention. Reports indicate that more than 3 million individuals worldwide suffer from pesticide poisoning each year due to various factors (Dwivedi et al., 2014). Acute pesticide poisoning, in particular, can inflict severe harm in a short time frame and may even be life-threatening. Cases of acute pesticide poisoning typically arise from either intentional self-harm or accidental exposure. Notably, there are between 350,000 and 440,000 instances of pesticide poisoning annually, accounting for approximately 30 % of global suicides (Ko et al., 2018; Sun et al., 2022).

Dichlorvos (DDVP) is a potent organophosphorus pesticide widely utilized for the management of crop diseases and insect infestations. However, numerous studies indicate that the presence of dichlorvos in both terrestrial and aquatic ecosystems poses an escalating threat to human and animal health (Saravanakumar et al., 2024). Exposure to DDVP can inflict significant damage to various organs and systems, including the respiratory (He et al., 2018), digestive (Trivedi et al., 2021), nervous (Gu et al., 2021), and reproductive (Saka et al., 2024) systems. The liver, a crucial organ responsible for metabolism,

* Correspondence to: 37 Guoxue Lane, Wuhou District, Chengdu, Sichuan, China.
*E-mail address:* tangwf@scu.edu.cn (W. Tang).
[1] These authors contributed equally to this study and share first authorship.

https://doi.org/10.1016/j.ecoenv.2025.117747
Received 7 October 2024; Received in revised form 9 January 2025; Accepted 13 January 2025
Available online 16 January 2025

detoxification, and immune regulation, is particularly vulnerable to pesticide exposure. Previous studies conducted on experimental animals have suggested a correlation between DDVP exposure and hepatotoxicity. Research indicates that liver toxicity caused by DDVP is multifaceted and includes oxidative stress, energy metabolism disruption, DNA damage, and apoptosis. For example, exposure of zebrafish to DDVP results in significant disruption of liver energy metabolism, inhibition of gene expression related to glucose metabolism, and modulation of the levels of molecules involved in reactive oxygen species (ROS) reactions and proteasomal degradation (Bui-Nguyen et al., 2015). Furthermore, DDVP exposure depletes the liver's antioxidant system, rendering cells and intracellular components vulnerable to attack by the ROS it generates (Ajiboye, 2010). This pesticide induces oxidative stress, leading to genetic instability and apoptosis, impairing gene transcription (Trivedi et al., 2021). However, the molecular pathways underlying these processes remain inadequately understood. This uncertainty regarding the mechanism of action in the liver presents a significant barrier to achieving favorable outcomes in patients suffering from DDVP poisoning.

Immunity-related GTPase M (IRGM) is an intracellular protein and a member of the IRG family. The IRG gene family comprises more than 20 members in mice and plays a critical role in regulating autophagy flux (Haldar et al., 2016). Notably, the only IRG family members present in humans are IRGM and IRGC (Biering et al., 2017). Jelena et al. reported that IRGM-deficient mice exhibited severe impairment of lysosomal function and significantly increased susceptibility to infection (Maric-Biresev et al., 2016). Many research efforts have highlighted that IRGM could be significant in the development of several liver disorders, such as nonalcoholic fatty liver disease and hepatic steatosis (Nath et al., 2021; Zhang et al., 2024; Bellini et al., 2017). However, the role of IRGM in pesticide-induced hepatotoxicity remains largely unexplored.

To date, acute exposure to DDVP remains a significant public health concern. A limited number of studies have concentrated on clarifying the molecular mechanisms that contribute to liver injury resulting from exposure to DDVP. In this study, we sought to investigate the response of hepatocytes after acute exposure to DDVP, focusing particularly on the development of oxidative stress, cell death, and possible interactions among these processes. Our results offer fresh perspectives on the molecular mechanisms underlying hepatotoxicity prompted by organophosphorus pesticides. Furthermore, by clarifying the role of IRGM in regulating cellular responses to DDVP exposure, we underscore IRGM as a promising therapeutic target for the prevention and treatment of DDVP-related liver disease.

## 2. Materials and methods

### 2.1. Animals

Wistar rats (240–260 g) were acquired from Beijing Vitong Lihua Experimental Animal Technology Co., Ltd. A 7-day environmental adaptation period was implemented prior to the commencement of the experiment. The rats were housed in standard animal rooms at a density of 3–4 per cage within the animal facility of Sichuan University, China. The Animal Experimentation Ethics Committee at Sichuan University granted approval for this protocol (animal authorization number: 20221230005). All animal experiments adhered to institutional and national guidelines, with all necessary measures taken to minimise both the number of animals used and their suffering. We procured DDVP (2,2-dichlorovinyl dimethyl phosphate) with a purity of 77.5 % from Shandong Dacheng Biochemical Co., Ltd. (Zibo, Shandong, China). Before the treatment commenced, the rats were assigned to groups at random, with each group consisting of 8 rats. DDVP was administered via intragastric injection at a single dose of 0, 30, 60, or 90 mg/kg diluted with physiological saline at a dosage of 4 ml/kg. For rapamycin treatment (Cat# S1039; Selleck), the rats received an intraperitoneal injection of 2 ml/kg every other day for 5 days, followed by a single gavage of DDVP on the sixth day. A model for overexpressing rat IRGM using adeno-associated virus serotype 8 (AAV8) was employed, with the AAV and vector for this AAV8-mediated expression supplied by Genetech Co., Ltd.

The concentration of DDVP in tissue samples was analyzed using high-performance liquid chromatography-mass spectrometry (HPLC-MS). To extract the compound, 1 ml of acetonitrile solution was added to 1 g of liver sample, followed by vortex mixing. The mixture was then subjected to ultrasonic extraction for 10 minutes. After extraction, the sample was placed in a high-speed refrigerated centrifuge set at 10,000 r/min and centrifuged for 5 minutes. The supernatant was then filtered through a microporous membrane and analyzed using ultra-high performance liquid chromatography coupled with mass spectrometry. The analysis was performed using a 1290 Infinity II-6470 system (Agilent Technologies Co., Ltd.) on a computer. A Venusil MP C18 chromatographic column (100 mm × 2.1 mm, 3 μm) was utilized, with a column temperature maintained at 40°C. The injection volume was set at 2 μL, and the flow rate was 0.3 ml/min. The mobile phase consisted of A: 0.1 % formic acid aqueous solution and B: acetonitrile, with the following gradient elution program: 0–3.0 min, 20–90 % B; 3.0–3.5 min, 90 % B; 3.5–3.51 min, 90–20 % B; and 3.51–5.0 min, 20 % B. The detection was conducted using ESI positive ion scanning with a multiple reaction monitoring (MRM) method. The curtain gas flow was set at 32 L/min, atomization gas at 50 L/min, auxiliary heating gas at 55 L/min, and the collision gas was set to medium. The auxiliary heating gas temperature was maintained at 300°C.

### 2.2. Cells

BRL-3A (CL-0036) cells were generously supplied by Wuhan Pricella Biotechnology Co., Ltd. (Wuhan, China) and were grown in DMEM (Ca# 41965062; Thermo) that was enriched with 10 % FBS (Cat# 10438026; Thermo) and 1 % penicillin/streptomycin (Cat# 15140148; Thermo). These cells were sustained in a mycoplasma-free environment within a humidified incubator set at 37 °C, providing a 5 % CO2 atmosphere. Identification of the cells was performed through STR analysis, and cultivation occurred in T-25 culture flasks (Corning, USA).

### 2.3. Antibodies and reagents

The host protein antibodies utilised in this study included anti-NRF2 (Cat# 163968–1-AP), anti-HO-1 (Cat# 10701–1-AP), anti-SLC7A11 (Cat# 26864–1-AP), anti-BCL2 (Cat# 26593–1-AP), and anti-BAX (Cat# 50599–2-Ig) antibodies, all of which were procured from Proteintech. The anti-cleaved caspase-3 (Cat# 9661) antibody was obtained from Cell Signaling Technology. Additionally, anti-P62 (Cat# ab91526) and anti-LC3 (Cat# ab63817) antibodies were obtained from Abcam. The anti-IRGM (Cat# 4543) antibody was purchased from ProSci, while the rabbit polyclonal monoclonal antibody against β-tubulin (Cat# B1031) was acquired from Biodragon. Further antibodies and stains, such as goat anti-rabbit Alexa Fluor 488 (Cat# ab150077), goat anti-mouse Alexa Fluor 488 (Cat# ab150113), and DAPI (Cat# ab104139), were sourced from Abcam.

Rapamycin (Cat# S1039, Selleck) was utilized to activate autophagic flux in order to assess whether the impairment of autophagy is a contributing factor to the liver function deterioration induced by DDVP. The following reagents were purchased from Gibco (MA, US): DMEM (Cat# 8123282), penicillin—streptomycin solution (Cat# 15140148), 0.25 % trypsin (Cat# 25200072), foetal bovine serum (FBS, Cat# a5669701), and phosphate-buffered saline (PBS, Cat# 10010001). Furthermore, kits for detecting malondialdehyde (MDA) (Cat# BC0025), reduced glutathione (GSH) (Cat# BC1175), catalase (CAT) activity (Cat# BCO205), total antioxidant capacity (T-AOC) (Cat# BC1315), and superoxide dismutase (SOD) activity (Cat# BC5165) were sourced from Beijing Solarbio Technology Co., Ltd. in China. Additionally, a glutathione peroxidase (GSH-PX) assay kit (Cat# A005–1–2) was acquired from the Nanjing Jiancheng Bioengineering Institute. A

prestained colour protein marker (Cat# P0069), ROS detection kit (Cat# S0033S), BCA protein detection reagent kit (Cat# P0012), and calcein—AM fluorescence probe (Cat# S0033S) were obtained from Beyotime Biotechnology Co., Ltd. (Nantong, China). Additionally, a TUNEL Apoptosis Detection Kit (Cat# HY-K1078) was procured from MedChemExpress (MCE, Shanghai, China).

### 2.4. Western blot

A RIPA solution was formulated with a protease inhibitor (PMSF, Solarbio). Liver tissues (1 ml/100 mg of tissue) or cells were immersed in RIPA buffer and sonicated in an ice-water mixture. Subsequently, the supernatant is collected after centrifugation by table centrifuge. Protein samples were heated at 95 °C for 10 min before being loaded onto Tris—glycine SDS polyacrylamide gel electrophoresis gels for separation, followed by transfer to polyvinylidene difluoride membranes. Following the incubation of the membrane with a 5 % serum blocking buffer, it was treated with a primary antibody overnight at 4 °C. The next day, the membrane was exposed to a secondary antibody at room temperature for one hour. Protein expression was determined via a chemiluminescence imaging system (Bio-Rad, CA), and ImageJ software was used to quantify protein expression, which was normalised to that of β-tubulin. The primary antibodies utilised in this study included rabbit anti-NRF2 (1:1500), rabbit anti-HO-1 (1:2000), rabbit anti-SLC7A11 (1:1000), rabbit anti-BCL2 (1:1500), rabbit anti-BAX (1:2000), rabbit anti-P62 (1:1000), rabbit anti-LC3 (1:500), rabbit anti-IRGM (1:500), and mouse anti-β-tubulin (1:4000) antibodies.

### 2.5. TUNEL assay

Apoptosis detection was performed via a TUNEL assay kit (Cat# HY-K1078, MCE) following the manufacturer's instructions. In brief, 4-μm-thick liver tissue sections were deparaffinised, rehydrated, and washed twice with PBS. Proteinase K digestion was then conducted for 10 min. Following two additional washes with PBS, the TUNEL working solution (5 μl of TdT enzyme and 45 μl of FITC-12-dUTP mixture) was applied, and the samples were kept for 60 min. After the samples were mounted on coverslips with anti-fluorescence quenching mounting medium containing DAPI (Cat# S2110, Solarbio), they were examined with a laser scanning confocal microscope (Nikon, Japan).

### 2.6. Histopathology and immunofluorescence staining

Rat livers were fixed with 4 % paraformaldehyde. Haemotoxylin and eosin (H&E) staining involves a sequence of dewaxing, debenzenisation, rehydration, staining, dehydration, and sealing. Liver pathology scores were assigned in a blinded manner by pathologists for each group on the basis of a minimum of five samples per group and at least five fields per sample. For immunofluorescence, the tissues were embedded, sectioned, deparaffinised, and rehydrated. The samples were then immersed in antigen retrieval solution and subjected to microwave antigen retrieval for 16 min to facilitate antigen exposure. Blocking was performed with 10 % foetal calf serum for 60 min at room temperature. The utilized primary antibodies comprised rabbit anti-P62 (1:200), rabbit anti-LC3 (1:100), and rabbit anti-cleaved caspase-3 (1:100), which were incubated with the tissues overnight at 4 °C. Following three washes with PBS, the secondary antibody conjugated to Alexa Fluor 488 (Cat# ab150077, 1:2000, Abcam, UK) was introduced, and the solution was incubated in the dark for 90 min. After conducting three more washes with PBS, the slides were prepared using an anti-fluorescence quenching mounting medium that includes DAPI (Cat# S2110, Solarbio). Imaging was carried out using a Leica DM2500 fluorescence microscope (Leica, Germany), and the resulting images were analyzed with ImageJ software (NIH, USA).

### 2.7. Transmission electron microscopy

Rat liver tissue was rapidly sliced into thin sections measuring less than 1–2 $mm^3$ , and the samples were preserved in a specialised electron microscopy fixative at 4 °C. Samples were consistently obtained from the same area of the organ. The blocks were subsequently fixed for electron microscopy using 2.5 % glutaraldehyde in 0.1 M methyl acetate buffer, followed by rinsing in the same buffer. The specimens were subsequently subjected to incubation in a 1 % solution of osmium tetroxide within a 0.1 M cacodylate buffer, and this was followed by dehydration using a series of graded alcohols and acetonitrile. Finally, the samples were embedded in epoxy resin, and images were acquired via transmission electron microscopy.

### 2.8. Quantitative polymerase chain reaction (qPCR)

Following the instructions provided by the reagent manufacturer (Vazyme Biotechnology Co., Ltd.), total RNA was extracted via an RNA extraction kit (Cat# R701, Vazyme), and cDNA was synthesised via a reverse transcription kit (Cat# wc-SJH0021, WCGENE). The qPCR was conducted in a 10 μl reaction system, which included mRNA Quantitative Master Mix (Cat# wc-SJH0002, WCGENE), cDNA, and specific primers, with a minimum of three replicates established for each group. The specific sequences of the primers used were as follows: Rat IRGM: forward primer 5′ -CAAACATCAGGTGCTGTGAAC-3′; reverse primer 5′ -AGTGCATTCACAGTTGTACAGG-3′; and rat GAPDH: forward primer 5′ -ATACGCACAGAGGAAACCAG-3′; reverse primer 5′ -TTCCTTGTTCAGCAACTGAGG-3′. For the qPCR array experiment, cDNA was mixed with WCGENE mRNA qPCR mix (WCGENE), and 9 μl of this mixture was added per well to the qPCR array plate (Cat# wc-mRNA0291-R, WCGENE). The plate was then centrifuged at 2000 rpm for 20 s in a desktop centrifuge, followed by detection. The relative mRNA expression levels were calculated via the $2^{-\Delta\Delta CT}$ method. The protocol for qPCR array analysis is detailed on the WCGENE website.

### 2.9. Transcriptome analysis

RNA sequencing was conducted on rat liver tissues from three groups, each consisting of six biological replicates. The quality of the RNA was assessed using an Agilent Bioanalyzer. RNA samples of high quality were chosen based on several criteria: OD 260/280 falling between 1.8 and 2.2, OD 260/230 being at least 2.0, and a minimum quantity of 1 μg. Subsequently, these samples were utilized to create a sequencing library that was sequenced using an Illumina HiSeq platform. The gene expression levels for each gene were determined using the transcripts per million method, facilitating the evaluation of gene expression. A functional enrichment analysis using the Kyoto Encyclopedia of Genes and Genomes (KEGG) database was conducted to identify pathways with differential activation.

### 2.10. Metabolome analysis

Analysis of the metabolome was performed by Zhongke New Life Biotechnology Co., Ltd. based in Shanghai, China, using six biological replicates for every group. After the liver samples underwent gradual thawing at 4 °C, a suitable volume of each sample was mixed with a precooled solution of water, acetonitrile, and methanol in a 1:2:2 ratio (v/v). This mixture was then vortexed and subjected to cryogenic sonication for 30 min before being allowed to stand at −20 °C for an additional 10 min. After that, the samples underwent centrifugation at 14,000 × g for 20 min, and then the supernatants were evaporated using a vacuum. For the purpose of mass spectrometry analysis, 100 μl of a 1:1 acetonitrile-water mixture (v/v) was introduced to reconstitute the dried samples, followed by vortexing and centrifugation at the same speed and temperature. The supernatant that had been prepared was used for metabolic analysis.

### 2.11. ROS detection

In a six-well plate (NEST), a total of $8 \times 10^5$ cells were placed in each well. Following the specified stimulation, an ROS detection kit (Cat# S0033S, Beyotime) was used to measure the levels of ROS in the cytoplasm. Briefly, after the original cell culture medium was removed, medium containing the DCFH-DA fluorescence probe was added. The cells were subsequently placed in a cell culture incubator at 37 °C for 20 min, followed by three washes with serum-free cell culture medium to remove any extracellular DCFH-DA. DCFH-DA can freely penetrate cells and is subsequently hydrolysed and oxidised into DCF, which emits fluorescence and cannot cross the cell membrane. Imaging was conducted using a Leica DM2500 fluorescence microscope (Leica, Germany).

### 2.12. Cell viability detection

In a 96-well plate (NEST), $1 \times 10^5$ cells were inoculated into each well and left to adhere for 8 hours. After the designated stimulation, the viability of cells was assessed using a Cell Counting Kit-8 (CCK-8) assay (Cat# HY-K0301, MCE). In summary, 10 μL of the CCK-8 solution was introduced to every well, mixed well, and incubated for 60 min in a cell culture incubator set at 37 °C. The optical density was assessed using a Tecan Spark Reader (Tecan Group Ltd., Switzerland) at a wavelength of 450 nm.

### 2.13. Statistical analysis

All the results are expressed as the means ± standard errors of the mean (SEMs). Statistical analyses and graphical presentations were conducted via IBM SPSS software (version 25.0) and GraphPad Prism 9.5.1 (GraphPad Software, USA). Analysis of variance and Student's t test were used for comparisons between groups, whereas the Shapiro—Wilk test was used to assess the normality of the data. The Mann—Whitney *U* test was applied to compare nonnormally distributed variables between two groups, and the Kruskal—Wallis test was used for comparisons among multiple groups with nonnormally distributed variables. Unless otherwise stated, significant differences between groups were evaluated using a one-way analysis of variance (ANOVA). P values less than.05 and.01 were considered statistically significant.

## 3. Results

### 3.1. Clinical symptoms and liver damage in Wistar rats due to acute DDVP poisoning

The DDVP acute poisoning model established through intragastric injection is illustrated in Fig. 1A. Compared with the normal control group, the DDVP poisoning groups (both low-dose and high-dose) presented significant increases in the secretion of viscous saliva, tremors in the limbs and trunk, respiratory distress, and faecal incontinence (data not shown). In severe cases, the affected rats experienced violent whole-body shaking and mental disturbances (data not shown). Notably, these symptoms peaked 30 min after intragastric administration and were markedly alleviated after 1–2 h. An excessively high toxic dose (90 mg/kg) resulted in the death of all the experimental rats within 10–30 min, which is why higher doses were not utilised (Fig. 1F-G). Serum levels of liver biomarkers were measured to assess the toxic effects of DDVP. As demonstrated in Fig. 1C-D, high-dose DDVP exposure for 6 h resulted in severe hepatotoxicity, and no significant differences from the controls were observed in the low-dose group. H&E staining was employed to evaluate liver histopathological changes. The results indicated that the livers of the poisoned group exhibited congestion, abnormal cellular morphology and cell necrosis (Fig. 1B). Furthermore, the hepatotoxicity of DDVP was corroborated by blinded pathology scoring (Fig. 1E). Additionally, transmission electron microscopy was used to observe

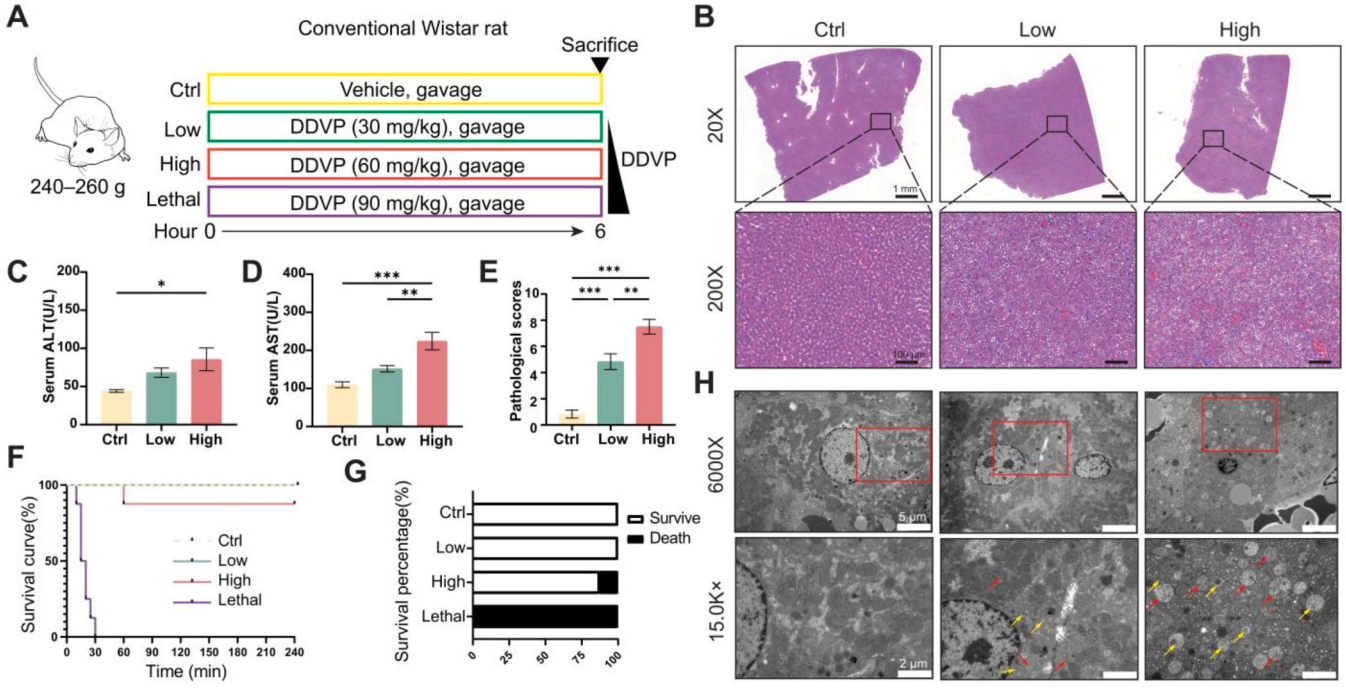


**Fig. 1.** Illustration of the significant hepatotoxicity associated with acute DDVP poisoning. (A) Schematic diagram depicting the experimental design of the Wistar rat DDVP exposure model. (B, E) The DDVP poisoning model is based on normal Wistar rats. Haemotoxylin and eosin staining shown (top, scale bar = 1 mm) and at 15,000 × magnification (bottom, scale bar = 100 μm), alongside corresponding pathological scores. (C-D) The expression levels of ALT and AST were determined for each group. (F-G) Survival curves and survival rates of the rats in each group are presented. (H) Transmission electron microscopy images at 6000 × (top, scale bar = 5 μm) and 15,000 × (bottom, scale bar = 2 μm) resolution were used to observe autophagosomes (highlighted by yellow arrows) and damaged mitochondria (highlighted by red arrows) in hepatocytes. * $P < .05$, * * $P < .01$, * ** $P < .001$.

alterations in the ultrastructures of liver cells. The findings revealed increased formation of autophagosomes following DDVP treatment, accompanied by mitochondrial swelling, outer membrane rupture, and fragmentation and dissolution of the mitochondrial cristae (Fig. 1H).

### 3.2. Acute DDVP poisoning leads to impaired hepatic autophagy

To further evaluate the role of autophagy in liver injury induced by DDVP exposure, we examined the expression of 90 genes involved in the autophagy pathway via a qPCR array. The results indicated that

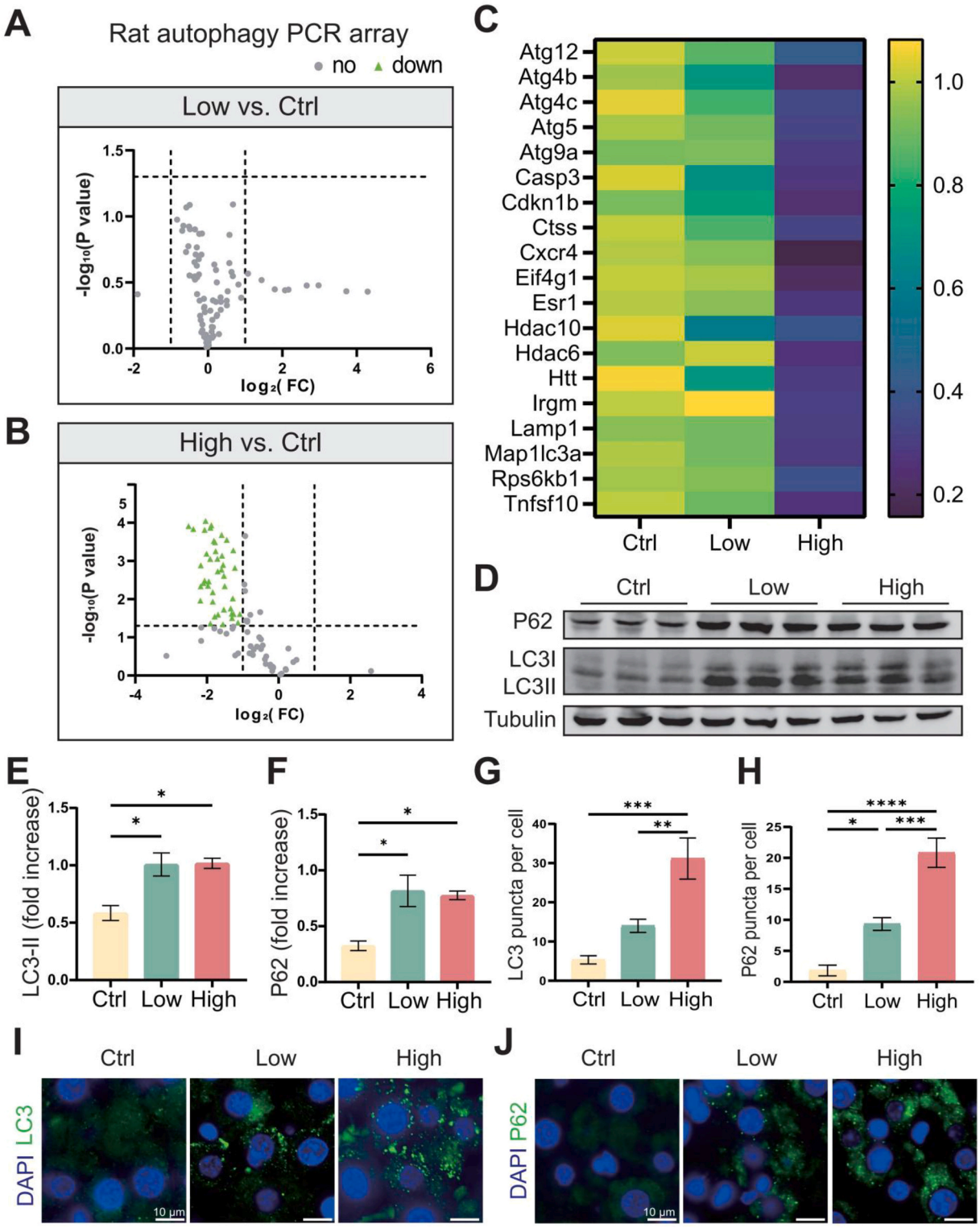


**Fig. 2.** DDVP disrupts hepatocyte autophagy. (A-C) Autophagy gene expression array based on rat autophagy qPCR array analysis. The volcano plot illustrates differentially expressed transcripts associated with autophagy (A-B), and these DEGs are detailed in the heatmap (C). (D-F) Western blot analysis of P62 and LC3 expression. (G-H) Quantification of the number of LC3-positive and P62-positive puncta per cell was performed via ImageJ. (I-J) Representative immunofluorescence confocal images depict LC3/P62-positive puncta (green) and DAPI (blue). Scale bar = 10 μm. * $P < .05$, * * $P < .01$, * ** $P < .001$.

significant changes in the expression of genes encoding autophagy-related proteins were observed only in the high-dose poisoning group, while no significant changes from the controls were detected in the low-dose poisoning group (Fig. 2A-C). The quantification of P62 and LC3-II is widely recognised as an effective measure of autophagic flux. Western blot analysis revealed that DDVP treatment increased the protein expression of P62 and LC3-II (Fig. 2D-F). Additionally, fluorescence microscopy analysis of liver tissue revealed a significant increase in the number of LC3 and P62 puncta following low-dose DDVP exposure, with an even greater increase in the high-dose group (Fig. 2G-J). Notably, the accumulation of P62, a marker of impaired autophagy flux, suggests that incomplete autophagy contributes to this process. Collectively, these data suggest that incomplete autophagy plays a role in liver injury induced by acute exposure to DDVP.

### 3.3. DDVP exposure induces liver oxidative stress by modulating the NRF2/HO-1 signalling pathway

Given that oxidative stress plays a crucial role in the pathogenesis of organophosphorus pesticide-induced liver injury (Berg et al., 2019), we hypothesise that acute exposure to DDVP may disrupt hepatic redox homeostasis. Consistent with our expectations, DDVP exposure led to an increase in the production of lipid peroxidation products, specifically MDA, while concurrently reducing the activity of enzymatic antioxidants such as SOD, CAT, and GSH-PX (Figure S1A). NRF2 and HO-1 are essential factors in the regulation of intracellular redox homeostasis. Compared with those in the control group, the protein expression levels of NRF2 and HO-1 in the livers of the high-dose group were significantly lower (Figure S1B). These findings suggest that DDVP induces hepatic redox imbalance through the modulation of the NRF2/HO-1 pathway.

### 3.4. Rapamycin prevents liver injury induced by acute exposure to DDVP

We utilised rapamycin, an autophagy activator, to investigate the role of autophagy in liver injury resulting from acute exposure to DDVP (Fig. 3A). Although rapamycin did not increase the survival rate of rats subjected to acute DDVP exposure, it mitigated liver toxicity (Fig. 3E-F). Furthermore, transmission electron microscopy analysis revealed that the administration of rapamycin effectively reduced the accumulation of swollen autophagosomes in liver cells affected by poisoning (Fig. 3B). Histopathological analysis indicated that rapamycin treatment mitigated the pathological deterioration induced by DDVP (Fig. 3C-D). Our findings also demonstrate that rapamycin influences DDVP-induced ferroptosis through regulation of the NRF2/HO-1 pathway (Fig. 3G-K). In summary, rapamycin helps prevent the occurrence of incomplete autophagy induced by DDVP, thereby alleviating the redox imbalance within the body and ultimately reducing liver damage.

### 3.5. DDVP induces incomplete autophagy and ferroptosis in BRL-3A cells

We continued to assess the in vitro cytotoxicity of DDVP. We employed the HPLC-MS method to analyze the components and concentration of DDVP in rat liver (Figure S2), which established a basis for selecting a concentration range of 1–64 μM for subsequent experiments. We utilized BRL-3A cells to establish an in vitro model and employed the CCK-8 assay to assess cell viability. The results demonstrated that DDVP decreased BRL-3A cell viability in a dose- and time-dependent manner (Fig. 4A-B). Furthermore, the cells were stained with calcein-AM, and the images revealed that the green fluorescence of the liver cells gradually diminished as the dose was increased, indicating that DDVP has significant cytotoxic effects (Fig. 4G-H). Additionally, DDVP stimulation led to a dose-dependent increase in the release of ALT and AST from hepatocytes (Fig. 4C-D). Given that DDVP induces ferroptosis in vivo, we hypothesised that DDVP may also exert similar effects on BRL-3A cells. To investigate this hypothesis, we employed a DCFH-DA molecular probe to further evaluate ROS generation at the cellular level. As anticipated, exposure to DDVP resulted in increased ROS accumulation in BRL-3A cells (Fig. 4E-F). Western blot analysis indicated that DDVP reduced the expression of IRGM and SLC7A11 while increasing the expression of P62 and HO-1. Collectively, these findings suggest that

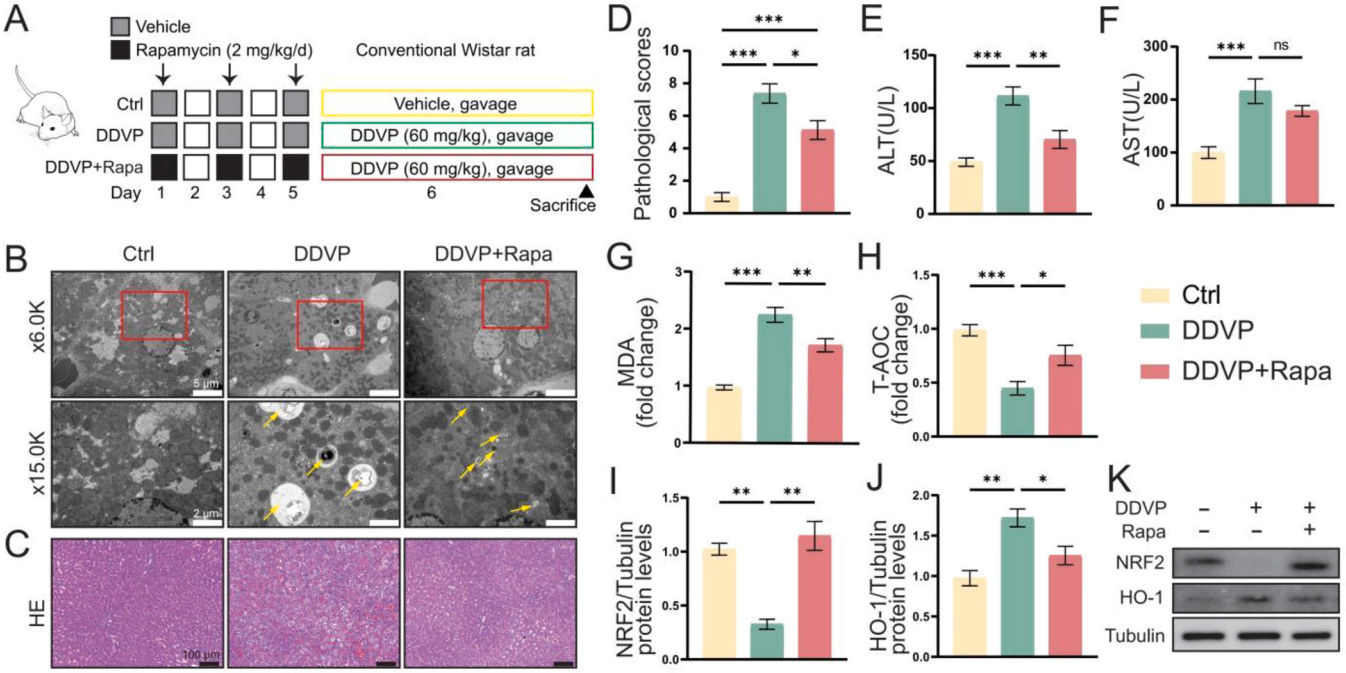


**Fig. 3.** Rapamycin alleviates DDVP-induced liver injury. (A) Schematic diagram illustrating the experimental design for rapamycin-treated Wistar rats exposed to DDVP. (B) Transmission electron microscopy images at 6000 × (top, scale bar = 5 μm) and 15000 × (bottom, scale bar = 2 μm) reveal the presence of autophagosomes (highlighted by yellow arrows) in hepatocytes. (C-D) Haematoxylin and eosin staining and pathological scoring are presented (scale bar = 100 μm). (E-F) The expression levels of ALT and AST were determined for each group. (G-H) ELISA was used to assess the T-AOC and MDA activity levels in each group. (I-K) Western blot analysis was conducted to evaluate the expression of NRF2 and HO-1. * $P < .05$, * * $P < .01$, * ** $P < .001$.

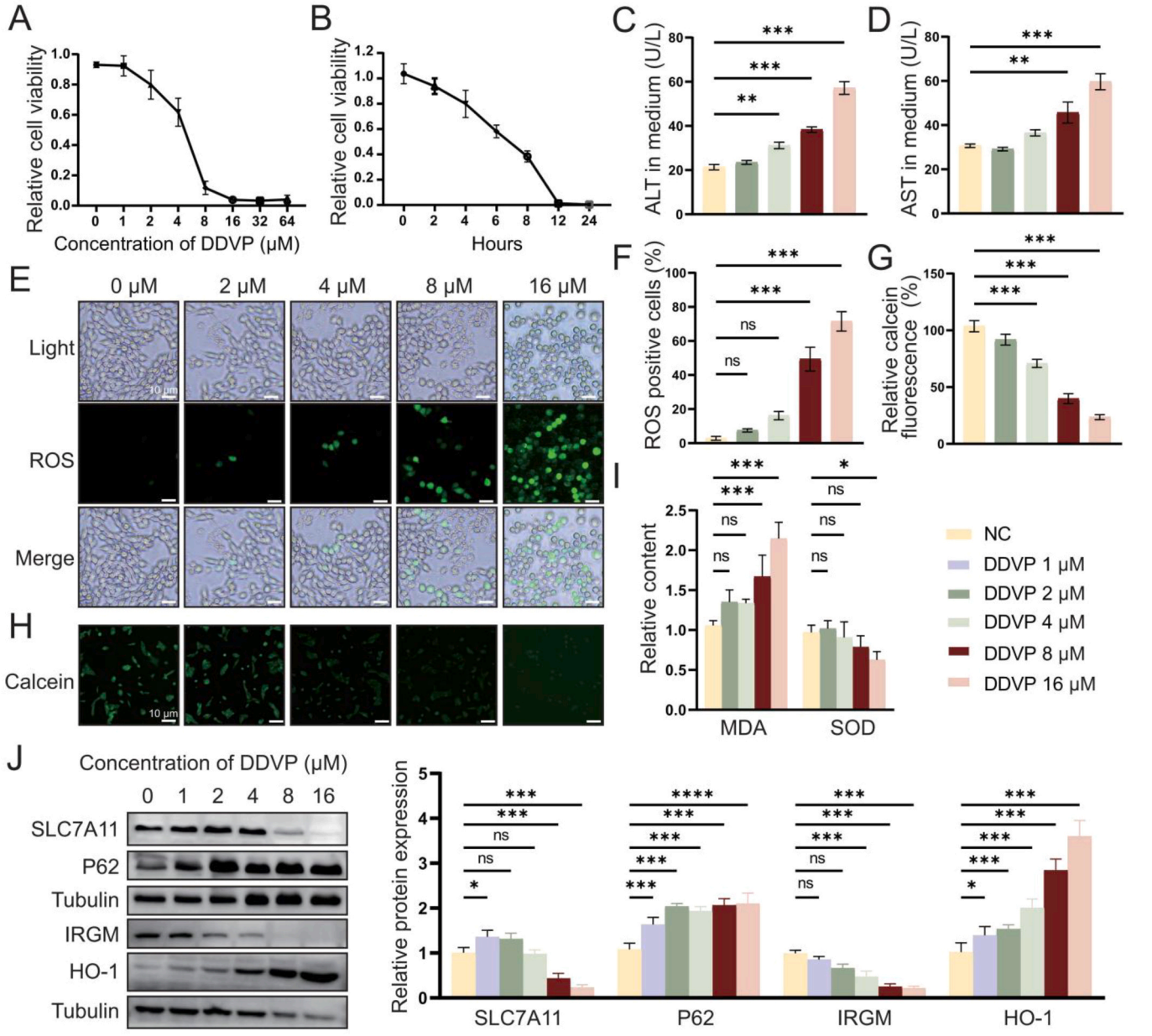


**Fig. 4.** IRGM mediates DDVP-induced damage in BRL-3A cells. (A) A CCK-8 assay was conducted after BRL-3A cells were treated with the specified concentration of DDVP for 12 h. (B) BRL-3A cells were exposed to 8 μM DDVP for the indicated durations for the CCK-8 assay. (C-D) The expression levels of ALT and AST were determined for each group. (E-F) Representative images illustrating ROS staining and the quantification of positive cells were acquired for every group. (G-H) Representative images of calcein-stained cells and an analysis of relative fluorescence intensity were performed for the cells in each group. (I) The expression levels of MDA and SOD in each group were measured using ELISA. Statistical comparisons were made using two-way ANOVA. (J) Western blot analysis was conducted to assess the expression of SLC7A11, P62, IRGM, and HO-1. Bar = 10 μm. Statistical comparisons were made using two-way ANOVA. * $P < .05$, * * $P < .01$, * ** $P < .001$, ns, not significant ($P > .05$).

DDVP exposure regulates autophagy signalling pathways and activates ferroptosis in vitro (Fig. 4I-J).

### 3.6. *Combined transcriptomic and metabolomic analyses reveal the effects of DDVP in the Liver*

Transcriptomic and metabolomic analysis was conducted to further elucidate the potential molecular mechanisms underlying liver injury in the DDVP exposure model. Principal component analysis (PCA) revealed distinct transcriptomic and metabolomic patterns among the different groups (Figs. 5A and 5D). In the transcriptomic analysis, we identified 365 differentially expressed genes (DEGs) with $|\log2FoldChange| > 1$ and P adj $< .05$, along with 1069 differentially abundant metabolites (DAMs), when the Ctrl group was compared with the DDVP group (Figs. 5B and 5E). The 50 genes with the most significant differences in expression are presented in Fig. 5C. Additionally, an analysis of KEGG pathway enrichment was conducted on the DEGs and DAMs to uncover pathways that exhibited significant enrichment as a result of DDVP exposure. In the transcriptomic analysis, numerous DEGs were enriched in the autophagy, apoptosis, and ferroptosis signalling pathways (Fig. 5F). Similarly, in the metabolome, many differentially abundant metabolites were significantly enriched in the biosynthesis of amino acids, ABC transporters, histidine metabolism, and arginine biosynthesis (Fig. 5G). We subsequently integrated the two -omics approaches to map the DEGs and DAMs jointly to KEGG pathways. The DEGs in DDVP-treated hepatocytes were enriched predominantly in ABC transporters,

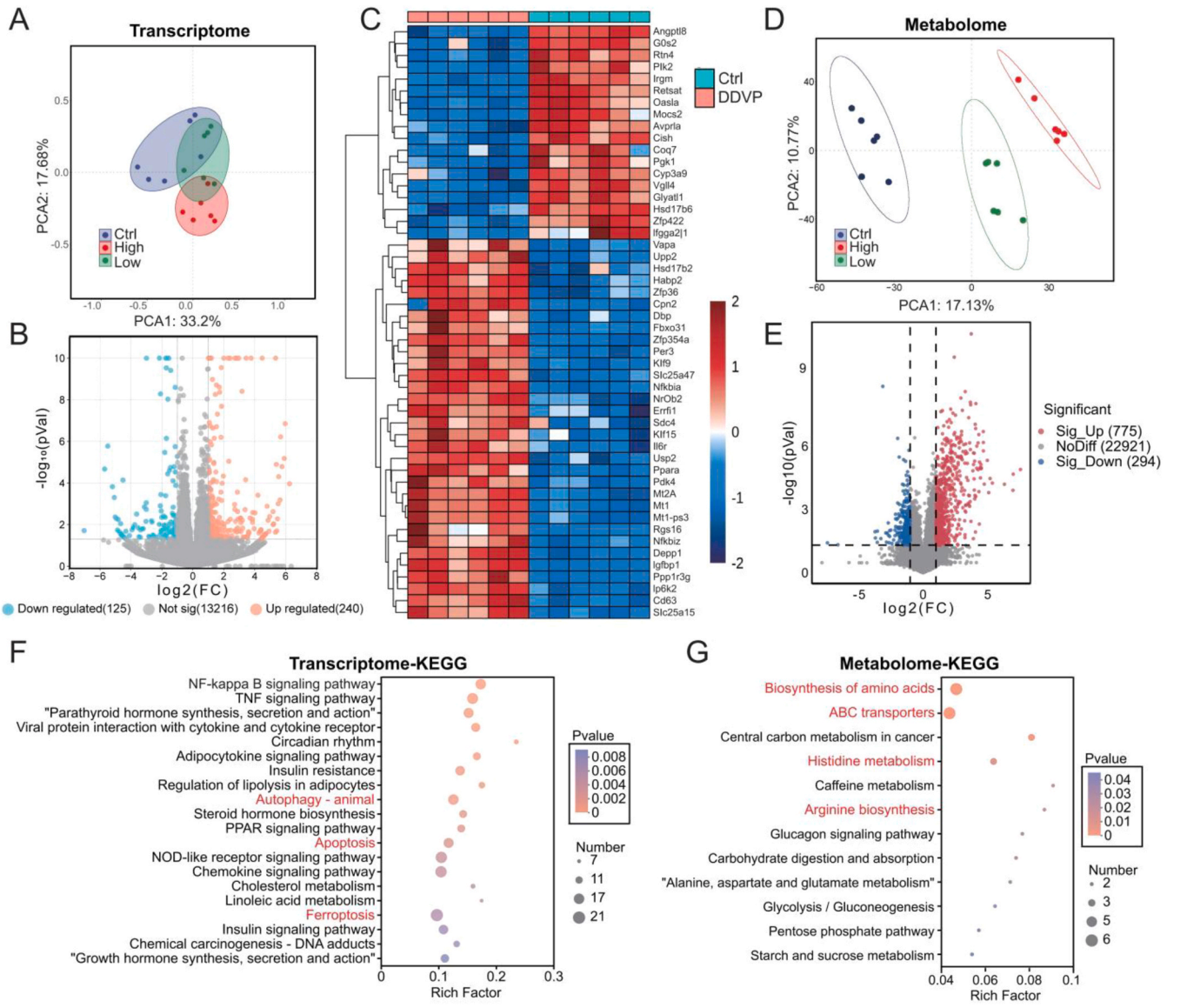


**Fig. 5.** Transcriptomic and metabolomic analyses elucidated the effects of DDVP on the liver. Comparison of liver tissue function between control and DDVP-treated rats. (A) Principal component analysis of the DEG dataset. (B) Volcano plot illustrating the differentially expressed transcripts. (C) Hierarchical clustering heatmap of the top 50 DEGs. (D) Principal component analysis of the DAMs within this dataset. (E) Volcano plot depicting the DAMs. (F) KEGG analysis of differential gene expression profiles derived from the transcriptomic analysis results. (G) KEGG analysis of differentially abundant metabolite profiles on the basis of metabolomic analysis results.

central carbon metabolism in cancer, amino sugar and nucleotide sugar metabolism, and purine metabolism (Figure S3A). The correlation between DEGs and DAMs was assessed via Pearson correlation analysis (Figure S3B).

Next, we performed gene set enrichment analysis for specific gene sets (Figure S4A). The genes that were more highly expressed in the DDVP poisoning group were significantly enriched in signalling pathways related to cellular energy metabolism, such as cellular respiration and glucose metabolism, as well as apoptosis signalling pathways. Conversely, the genes with downregulated expression in the poisoning group were enriched primarily in the mitochondrial respiratory chain, fatty acid metabolism, and carbohydrate biosynthesis processes. These findings align with previous reports indicating an imbalance in liver cell survival, energy metabolism, and apoptosis gene programs induced by DDVP (Bui-Nguyen et al., 2015). Additionally, we screened the top DEGs associated with autophagy, apoptosis, and oxidative stress-related pathways, mapped STRING data to extract protein—protein interaction data, and ultimately utilised Cytoscape software (version 3.10.0) for integration and visual analysis (Figure S4B). Collectively, our findings suggest that the hepatotoxicity of DDVP is at least partially linked to the regulation of hepatocyte metabolism and cell death.

### *3.7. DDVP induces hepatocyte apoptosis and reduces the expression of IRGM in vivo*

We subsequently investigated the role of DDVP in inducing hepatocyte apoptosis. The DEGs involved in the apoptosis pathway are illustrated in heatmaps (Fig. 6A). Compared with those in the Ctrl group, the liver cell nuclei in the poisoning group exhibited a significant increase in TUNEL-positive cells, indicating the occurrence of apoptosis (Fig. 6B). To further elucidate the proapoptotic effect of DDVP, we used immunofluorescence and Western blot analysis to assess apoptosis-related indicators. The results revealed a significant increase in the expression of the proapoptotic factors BAX and cleaved caspase 3, whereas the expression of the apoptosis-inhibiting factor BCL2 decreased in the poisoning group (Fig. 6C-D).

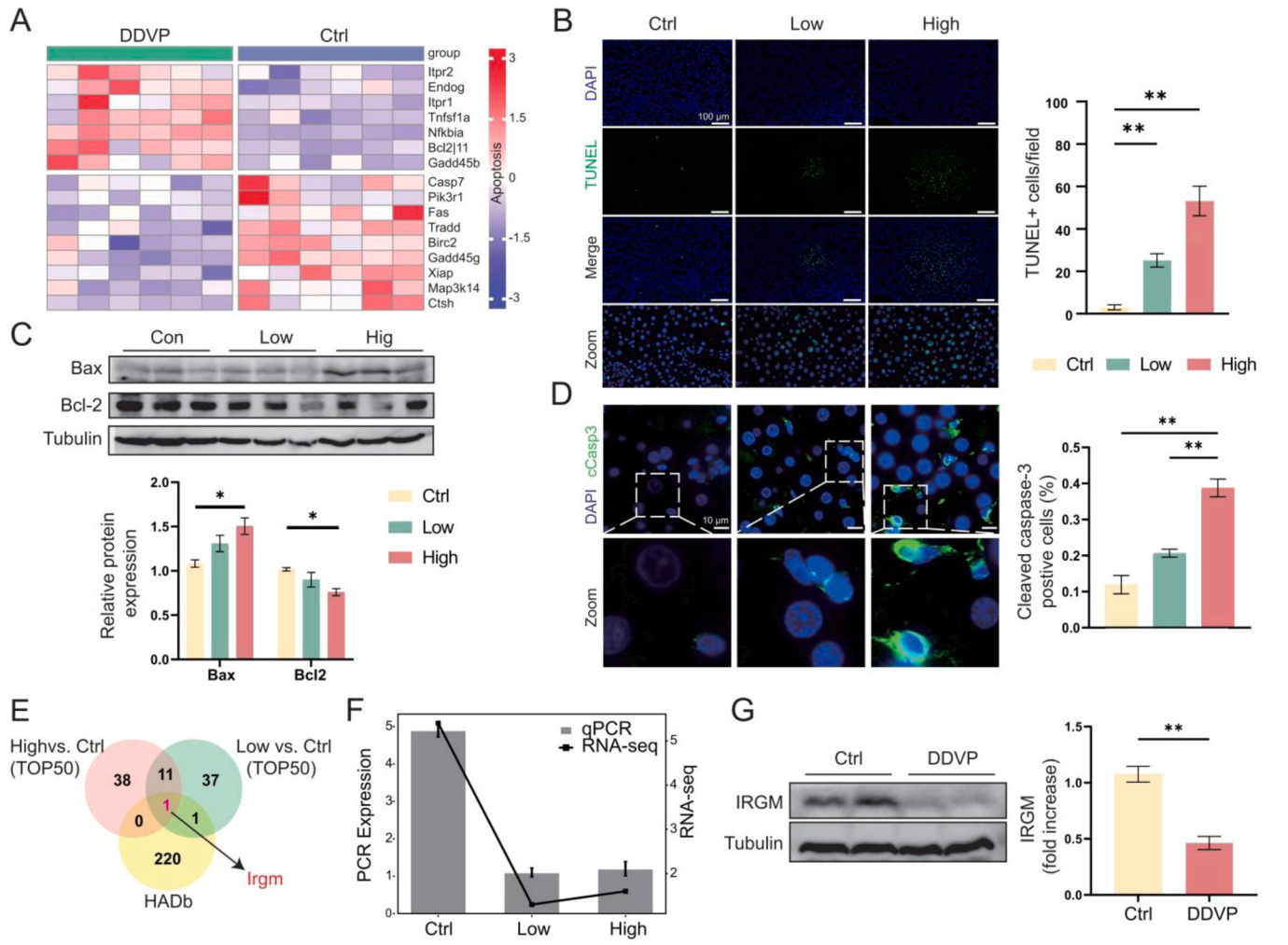


**Fig. 6.** DDVP treatment downregulates hepatic IRGM expression and induces hepatocyte apoptosis. (A) A heatmap illustrating differential gene expression in the apoptosis pathway. (B) Images representing TUNEL staining in liver tissue sections, accompanied by the quantification of TUNEL-positive cells, were determined by counting the TUNEL-positive cells in every area. (C) Western blot analysis of BAX and BCL2 expression. Statistical comparisons were made using two-way ANOVA. (D) Representative immunofluorescence images and quantification of cleaved caspase-3 staining (green) and DAPI (blue) in liver tissue sections. (E) A Venn diagram depicting overlapping significantly differentially expressed genes. (F) qPCR analysis of IRGM mRNA expression levels. (G) Western blot analysis of IRGM protein expression levels. Statistical comparisons were made using the two-tailed Student's t -test. * $P < .05$, * * $P < .01$.

Previous studies have demonstrated that autophagy and apoptosis can occur concurrently within a cell and that there is cross-talk between these two processes, as autophagy often precedes apoptosis (Peng et al., 2016). Additionally, some research has suggested that alterations in autophagy activity may represent an upstream event, where insufficient autophagy ultimately leads to apoptosis (Chen et al., 2022). In our investigation, we found that modulating autophagy mitigated liver injury, suggesting that incomplete autophagy may be a crucial upstream event in DDVP-induced liver injury. To further elucidate the mechanism underlying incomplete autophagy, we examined the differential expression of autophagy genes by integrating genes that are differentially expressed following poisoning with autophagy-related genes (ARGs) sourced from the Human Autophagy Database (HADb). The HADb houses a comprehensive collection of 222 ARGs. By analysing the intersections of the top 50 significantly DEGs and ARGs, we identified the candidate gene IRGM (Fig. 6E). Standard qPCR analysis corroborated the findings from the qPCR array and RNA-seq analysis, revealing a lack of Irgm mRNA expression (Figs. 6F and 2C). Furthermore, Western blot analysis revealed low IRGM protein expression levels in the liver tissues of the poisoning group (Fig. 6G).

### *3.8. AAV8-mediated IRGM overexpression alleviates DDVP-induced liver injury and incomplete autophagy*

The role of IRGM in DDVP-induced liver injury was subsequently evaluated in a DDVP poisoning model in which AAV8-mediated IRGM was overexpressed. Western blot analysis indicated that the successful injection of AAV8-IRGM via the hepatic portal vein resulted in the overexpression of IRGM in liver tissues (Fig. 7F). Surprisingly, this overexpression of IRGM prevented DDVP-induced incomplete autophagy (Fig. 7C-E). Additionally, H&E staining demonstrated that IRGM overexpression effectively alleviated DDVP-induced pathological damage (Fig. 7B). Transmission electron microscopy revealed that no macroautophagic vacuoles formed in the overexpression group (Fig. 7A). To assess cell apoptosis, we conducted immunofluorescence staining for TUNEL and cleaved caspase 3 expression (Fig. 7G-J). Consistently, the number of TUNEL-positive cells and the percentage of cleaved caspase-3-expressing cells significantly increased following exposure to DDVP. Conversely, the overexpression of IRGM significantly decreased both TUNEL-positive and cleaved caspase-3-expressing cell counts. Additionally, Western blot analysis demonstrated that IRGM overexpression led to a reduction in P62 expression, thereby decreasing apoptosis and ferroptosis (Fig. 7K-L). Collectively, these findings suggest that the

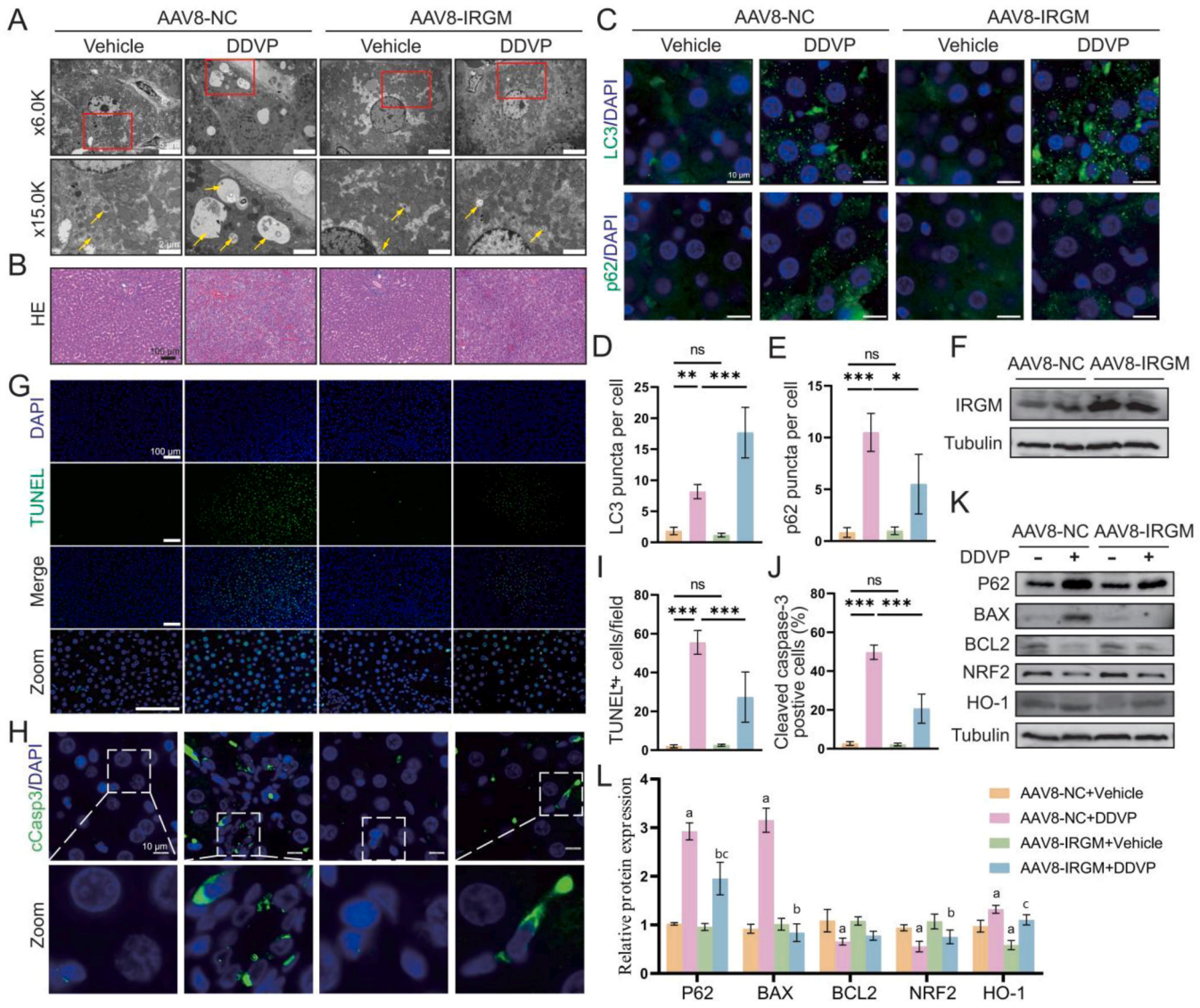


**Fig. 7.** AAV8-mediated overexpression of IRGM mitigates DDVP-induced liver injury and incomplete autophagy. (A) Observations were conducted via transmission electron microscopy at magnifications of 6000 × (top, scale bar = 5 μm) and 15000 × (bottom, scale bar = 2 μm). Autophagosomes (highlighted by yellow arrows) are visible in the cells. (B) Haemotoxylin and eosin staining analysis is shown (scale bar = 100 μm). (C) A representative immunofluorescence confocal image illustrates LC3/P62-positive puncta (green) alongside DAPI (blue). (D-E) Quantitative analysis of the number of LC3-positive and P62-positive spots per cell was performed via ImageJ. (F, K, L) Western blot analysis was conducted to assess the expression of IRGM, P62, BAX, BCL2, NRF2, and HO-1. a represents $P < .05$ compared with the AAV8-NC+Vehicle group; b represents $P < .05$ compared with the AAV8-NC+DDVP group; c represents $P < .05$ compared with the AAV8-IRGM+Vehicle group. Statistical comparisons were made using two-way ANOVA. (G, I) Representative images of TUNEL-stained liver tissue sections, along with quantification of positive cells, as calculated by counting TUNEL-positive cells in each area. (H, J) Representative immunofluorescence images and quantification of cleaved caspase-3 staining (green) and DAPI (blue) in liver tissue sections. * $P < .05$, * * $P < .01$, * ** $P < .001$, ns, not significant ($P > .05$). Group sizes: AAV8-NC+Vehicle ($n = 6$ rats), AAV8-NC+DDV*P* ($n = 6$), AAV8-IRGM+Vehicle ($n = 8$), AAV8-IRGM+DDVP ($n = 8$).

overexpression of IRGM mitigates the effects of incomplete autophagy and alleviates liver injury induced by DDVP.

## 4. Discussion

Our study demonstrates that DDVP induces the generation of ROS and incomplete autophagy, ultimately resulting in ferroptosis and apoptosis. DDVP induces incomplete autophagy by depleting IRGM protein expression, which further exacerbates the accumulation of ROS. Incomplete autophagy precedes ferroptosis and apoptosis, as the activation of the autophagy pathway through rapamycin partially mitigates cell death. IRGM is a critical molecule in DDVP-induced liver injury and plays a significant role in DDVP-induced hepatotoxicity. Our findings provide novel insights into the mechanisms underlying pesticide-related injuries and contribute to the development of effective treatments and preventive strategies against DDVP-induced liver injury.

Exposure to pesticides can have adverse effects on biota human health. The damage to nontarget organisms is diverse and depends on the type of pesticide, the dose, and the mode of exposure. Previous research has demonstrated that mice consuming beans treated with DDVP and fenitrothion exhibited degenerative changes in the liver (Somiael and Madiha, 2012). DDVP exposure can induce oxidative stress and apoptosis in both rats and *Channa punctatus* (Trivedi et al., 2021; Jalili et al., 2022). Furthermore, exposure to DDVP has been associated with an increased risk of liver injury in humans (Cecchi et al., 2012; Saka et al., 2021). While DDVP is clearly hepatotoxic, the specific molecular mechanisms underlying its liver-damaging effects remain poorly understood.

Ferroptosis, a form of programmed cell death that differs from conventional mechanisms like autophagy, apoptosis, and necrosis, is marked by disturbances in iron metabolism and an increase in lipid peroxides. The production of ROS along with the rise of lipid peroxides are critical elements that can trigger ferroptosis (Deng et al., 2021). This process has been demonstrated to play a significant role in cell death resulting from exposure to various environmentally hazardous substances, such as ethyl carbamate (Xu et al., 2022). The liver, the primary organ for iron storage, is crucial for maintaining iron metabolism and balance. SLC7A11 has been recognised as an important regulator of ferroptosis, as it negatively modulates the expression level of the downstream protein HO-1 and influences the ferroptosis process (Tang et al., 2021). While HO-1 exerts a cytoprotective effect at normal expression levels, its overactivation leads to the production of excessive ROS, thereby inducing ferroptosis (Mossakowska et al., 2022). Our research indicated a reduction in the protein expression levels of SLC7A11 within the poisoning group, while an increase in the expression of HO-1 was observed. This implies that both SLC7A11 and HO-1 play a role in the regulation of ferroptosis in hepatocytes induced by DDVP.

Incomplete autophagy is an abnormal autophagic response that occurs in cells and has garnered increasing attention from researchers in recent years. This phenomenon refers to a blockage in the intracellular autophagy pathway, whereby accumulated autophagosomes and lysosomes fail to undergo effective fusion and degradation, ultimately leading to cell death (Shao et al., 2021; Chen et al., 2014). For example, exposure to neferine (Xu et al., 2018), cadmium (Wang et al., 2019), and ammonia (Lu et al., 2019) has been shown to induce incomplete autophagy in cells. Factors such as damage to the actin cytoskeleton and microtubules, inhibition of GTPases and SNAREs, and impairment of lysosomal function may contribute to the occurrence of incomplete autophagy (Zhang et al., 2022). Furthermore, incomplete autophagy is implicated in the onset and progression of various human diseases, including cardiovascular diseases, neurodegenerative disorders, digestive system diseases, and cancer (Zhang et al., 2022). P62 and LC3 expression are established markers that reflect autophagy activity and are commonly employed to evaluate autophagy flux. A decrease in P62 expression alongside an accumulation of LC3 typically indicates an increase in autophagic flux, whereas a simultaneous increase in both markers suggests a blockage in autophagy flow (Qiu et al., 2014; Kim et al., 2020). A recent study demonstrated that DDVP induces the autophagy system in the hippocampus and cerebral cortex (Ommati et al., 2024). In our investigation, electron microscopy revealed an increase in autophagosome formation in the poisoning group, with the high-dose poisoning group exhibiting the production of large autophagic vacuoles. Furthermore, immunofluorescence and Western blotting analyses revealed that the expression levels of P62 and LC3 were altered, suggesting a reduction in hepatocyte autophagic flux during toxic injury. Notably, rapamycin was found to ameliorate DDVP-induced liver injury, further supporting the notion that toxic injury is autophagy dependent. In conclusion, our study provides the first evidence that DDVP effects are characterised by incomplete autophagy in liver cells.

IRGM is the only GTPase directly associated with human immunity and has significant effects on autophagy, cell death, and mitochondrial morphology (Singh et al., 2010). It regulates autophagy both directly and indirectly, playing a crucial role across the entire autophagy process (Goswami et al., 2022). Moreover, IRGM can activate the autophagy system to eliminate intracellular pathogens (Singh et al., 2010; Yang et al., 2022). Additionally, it has been reported that IRGM influences autophagy by regulating lysosomal biogenesis (Maric-Biresev et al., 2016). In our study, exposure to DDVP resulted in a concentration-dependent reduction in the mRNA and protein expression levels of IRGM. Data obtained from the use of adeno-associated viruses to target hepatocytes indicate that elevated IRGM expression can mitigate hepatotoxic damage in rats. Consequently, lysosomal dysfunction resulting from IRGM expression deficiency may mediate DDVP-induced incomplete autophagy in hepatocytes. While testing this hypothesis is beyond our current scope, it warrants further investigation in future research. In conclusion, our experiments demonstrate that incomplete autophagy occurs in hepatocytes exposed to DDVP and precedes ferroptosis and apoptosis, and that IRGM at least partially mediates the occurrence of this incomplete autophagy.

Pesticides have been recognised as inducers of oxidative stress, and mitochondria serve as primary targets of pesticide-induced damage. This interaction significantly impacts cellular energy metabolism and contributes to oxidative stress (Schmitt et al., 2021). Oxidative stress adversely affects intracellular organelles, such as mitochondria, as well as macromolecules, including proteins. Autophagy plays a crucial role in clearing damaged cellular components, thereby mitigating the detrimental effects of oxidative stress (Ruart et al., 2019). Generally, the accumulation of ROS can trigger either autophagy or cell death. Conversely, activated autophagy can reduce oxidative stress and cell death by inhibiting the production of ROS (Choi et al., 2022). However, in instances of incomplete autophagy, oxidative stress may further impede autophagic flux (Hu et al., 2016; Ma et al., 2015). Our data indicate that DDVP induces the accumulation of ROS in the liver. It is reasonable to conclude that the incomplete autophagy induced by DDVP undermines this protective cellular mechanism against oxidative damage. Moreover, oxidative stress exacerbates the effects of incomplete autophagy, ultimately leading to cell death.

Autophagy plays a central role in various cellular functions, including the regulation of oxidative stress, cellular metabolism, and programmed cell death (Gao et al., 2021). Recent studies have demonstrated that autophagy can act as an upstream regulatory pathway for a range of diseases, suggesting potential for the development of new therapeutic strategies by assessing the relevance of autophagy in different pathological contexts. For example, the autophagy agonist rapamycin has been shown to attenuate postseptic renal tubular apoptosis, whereas the autophagy inhibitor 3-MA exacerbates damage (Sun et al., 2021). Our findings indicate that DDVP-induced oxidative stress and cell death in hepatocytes can be mitigated by promoting autophagy, suggesting that restoring autophagic flux may serve as an effective strategy to alleviate DDVP hepatotoxicity. Furthermore, there is potential for the development of new drugs that target IRGM to modulate autophagy, thereby preventing damage from DDVP exposure, which holds practical significance.

## CRediT authorship contribution statement

**Wenfu Tang:** Writing – review & editing, Supervision, Methodology, Funding acquisition, Conceptualization. **Zixian Zhou:** Writing – original draft, Investigation, Formal analysis, Conceptualization. **Jiaqi Yao:** Writing – original draft, Methodology, Data curation. **Pengcheng Zhang:** Writing – original draft, Methodology, Data curation, Conceptualization. **Xianlin Zhao:** Writing – original draft, Methodology, Investigation. **Lv Zhu:** Writing – original draft, Software, Formal analysis. **Meihua Wan:** Writing – review & editing, Supervision, Conceptualization. **Ling Liu:** Writing – review & editing, Conceptualization. **Yuhong Jiang:** Writing – original draft, Investigation, Data curation. **Hang Lei:** Writing – original draft, Software, Formal analysis. **Zhijun Xie:** Writing – original draft, Methodology, Investigation. **Juan Li:** Writing – original draft, Methodology, Investigation.

## Declaration of Competing Interest

The authors declare the following financial interests/personal relationships which may be considered as potential competing interests: Wenfu Tang reports financial support was provided by the National Natural Science Foundation of China. If there are other authors, they declare that they have no known competing financial interests or personal relationships that could have appeared to influence the work reported in this paper.

## Acknowledgements

The authors are grateful to American Journal Experts (AJE) for their assistance with language editing. This work was supported by the National Natural Science Foundation of China [Grant no. 81603519 and 82174264]; and the Natural Science Foundation of Sichuan [Grant no. 23NSFSC2951].

## Appendix A. Supporting information

Supplementary data associated with this article can be found in the online version at doi:10.1016/j.ecoenv.2025.117747.

## Data availability

Data will be made available on request.

## References

Ajiboye, T.O., 2010. Redox status of the liver and kidney of 2,2-dichlorovinyl dimethyl phosphate (DDVP) treated rats. Chem. -Biol. Interact. 185, 202–207. https://doi.org/10.1016/j.cbi.2010.03.022.

Bellini, G., Miraglia Del Giudice, E., Nobili, V., Rossi, F., 2017. The IRGM rs10065172 variant increases the risk for steatosis but not for liver damage progression in Italian obese children. J. Hepatol. 67, 653–655. https://doi.org/10.1016/j.jhep.2017.02.037.

Berg, Z.K., et al., 2019. Association between occupational exposure to pesticides and cardiovascular disease incidence: the kuakini honolulu heart program. J. Am. Heart Assoc. 8, e012569. https://doi.org/10.1161/jaha.119.012569.

Biering, S.B., et al., 2017. Viral replication complexes are targeted by LC3-guided interferon-inducible GTPases. e77 Cell host Microbe 22, 74–85. https://doi.org/10.1016/j.chom.2017.06.005.

Brown, J.B., et al., 2021. An integrated host-microbiome response to atrazine exposure mediates toxicity in Drosophila. Commun. Biol. 4, 1324. https://doi.org/10.1038/s42003-021-02847-y.

Bui-Nguyen, T.M., et al., 2015. Dichlorvos exposure results in large scale disruption of energy metabolism in the liver of the zebrafish, Danio rerio. BMC Genom. 16, 853. https://doi.org/10.1186/s12864-015-1941-2.

Cecchi, A., Rovedatti, M.G., Sabino, G., Magnarelli, G.G., 2012. Environmental exposure to organophosphate pesticides: assessment of endocrine disruption and hepatotoxicity in pregnant women. Ecotoxicol. Environ. Saf. 80, 280–287. https://doi.org/10.1016/j.ecoenv.2012.03.008.

Chen, W., et al., 2022. Pharmacological manipulation of macrophage autophagy effectively rejuvenates the regenerative potential of biodegrading vascular graft in aging body. Bioact. Mater. 11, 283–299. https://doi.org/10.1016/j.bioactmat.2021.09.027.

Chen, X., et al., 2014. Coronavirus membrane-associated papain-like proteases induce autophagy through interacting with Beclin1 to negatively regulate antiviral innate immunity. Protein Cell 5, 912–927. https://doi.org/10.1007/s13238-014-0104-6.

Choi, S., et al., 2022. Diclofenac: a nonsteroidal anti-inflammatory drug inducing cancer cell death by inhibiting microtubule polymerization and autophagy flux. Antioxid. (Basel, Switz. ) 11. https://doi.org/10.3390/antiox11051009.

Deng, F., et al., 2021. The gut microbiota metabolite capsiate promotes Gpx4 expression by activating TRPV1 to inhibit intestinal ischemia reperfusion-induced ferroptosis. Gut Microbes 13, 1–21. https://doi.org/10.1080/19490976.2021.1902719.

Dwivedi, N., Flora, G., Kushwaha, P., Flora, S.J., 2014. Alpha-lipoic acid protects oxidative stress, changes in cholinergic system and tissue histopathology during co-exposure to arsenic-dichlorvos in rats. Environ. Toxicol. Pharmacol. 37, 7–23. https://doi.org/10.1016/j.etap.2013.10.010.

Ebel, A.V., et al., 2021. Association of agricultural, occupational, and military inhalants with autoantibodies and disease features in US veterans with rheumatoid arthritis. Arthritis Rheumatol. 73, 392–400. https://doi.org/10.1002/art.41559.

Gao, J., et al., 2021. Oroxylin A is a severe acute respiratory syndrome coronavirus 2-spiked pseudotyped virus blocker obtained from Radix Scutellariae using angiotensin-converting enzyme II/cell membrane chromatography. Phytother. Res.: PTR 35, 3194–3204. https://doi.org/10.1002/ptr.7030.

Goswami, A.B., Karadarević, D., Castaño-Rodríguez, N., 2022. Immunity-related GTPase IRGM at the intersection of autophagy, inflammation, and tumorigenesis. Inflamm. Res.: Off. J. Eur. Histamine Res. Soc. 71, 785–795. https://doi.org/10.1007/s00011-022-01595-x.

Gu, Y., et al., 2021. Dichlorvos poisoning caused chicken cerebrum tissue damage and related apoptosis-related gene changes. Sci. Total Environ. 783, 147051. https://doi.org/10.1016/j.scitotenv.2021.147051.

Haldar, A.K., et al., 2016. Chlamydia trachomatis Is Resistant to Inclusion Ubiquitination and Associated Host Defense in Gamma Interferon-Primed Human Epithelial Cells. mBio 7. https://doi.org/10.1128/mBio.01417-16.

He, F., et al., 2018. Xuebijing injection induces anti-inflammatory-like effects and downregulates the expression of TLR4 and NF-κB in lung injury caused by dichlorvos poisoning. Biomed. Pharmacother. = Biomed. Pharmacother. 106, 1404–1411. https://doi.org/10.1016/j.biopha.2018.07.111.

Hu, W., et al., 2016. Rotenone induces apoptosis in human lung cancer cells by regulating autophagic flux. IUBMB Life 68, 388–393. https://doi.org/10.1002/iub.1493.

Jalili, C., Farzaei, M.H., Rashidi, I., Mohammadnezamian, A., Ghanbari, A., 2022. Royal jelly protects dichlorvos liver-induced injury in male Wistar rats. Res. Pharm. Sci. 17, 209–218. https://doi.org/10.4103/1735-5362.335178.

Kim, K.W., Cho, H.J., Khaliq, S.A., Son, K.H., Yoon, M.S., 2020. Comparative analyses of mTOR/Akt and muscle atrophy-related signaling in aged respiratory and gastrocnemius muscles. Int. J. Mol. Sci. 21. https://doi.org/10.3390/ijms21082862.

Ko, S., et al., 2018. The burden of acute pesticide poisoning and pesticide regulation in Korea. J. Korean Med. Sci. 33, e208. https://doi.org/10.3346/jkms.2018.33.e208.

Lu, K., et al., 2019. Hepatic encephalopathy is linked to alterations of autophagic flux in astrocytes. EBioMedicine 48, 539–553. https://doi.org/10.1016/j.ebiom.2019.09.058.

Ma, Y.M., Han, W., Li, J., Hu, L.H., Zhou, Y.B., 2015. Physalin B not only inhibits the ubiquitin-proteasome pathway but also induces incomplete autophagic response in human colon cancer cells in vitro. Acta Pharmacol. Sin. 36, 517–527. https://doi.org/10.1038/aps.2014.157.

Maric-Biresev, J., et al., 2016. Loss of the interferon-γ-inducible regulatory immunity-related GTPase (IRG), Irgm1, causes activation of effector IRG proteins on lysosomes, damaging lysosomal function and predicting the dramatic susceptibility of Irgm1-deficient mice to infection. BMC Biol. 14, 33. https://doi.org/10.1186/s12915-016-0255-4.

Megharaj, M., Ramakrishnan, B., Venkateswarlu, K., Sethunathan, N., Naidu, R., 2011. Bioremediation approaches for organic pollutants: a critical perspective. Environ. Int. 37, 1362–1375. https://doi.org/10.1016/j.envint.2011.06.003.

Mossakowska, B.J., et al., 2022. Mechanisms of resistance to photodynamic therapy (PDT) in vulvar cancer. Int. J. Mol. Sci. 23. https://doi.org/10.3390/ijms23084117.

Nath, P., et al., 2021. IRGM links autoimmunity to autophagy. Autophagy 17, 578–580. https://doi.org/10.1080/15548627.2020.1810920.

Ommati, M.M., et al., 2024. Pesticide-induced alterations in locomotor activity, anxiety, and depression-like behavior are mediated through oxidative stress-related autophagy: a persistent developmental study in mice. J. Agric. Food Chem. 72, 11205–11220. https://doi.org/10.1021/acs.jafc.4c02299.

Peng, J., et al., 2016. Wild-type rabies virus induces autophagy in human and mouse neuroblastoma cell lines. Autophagy 12, 1704–1720. https://doi.org/10.1080/15548627.2016.1196315.

Qiu, W., et al., 2014. Tetrandrine blocks autophagic flux and induces apoptosis via energetic impairment in cancer cells. Cell Death Dis. 5, e1123. https://doi.org/10.1038/cddis.2014.84.

Ruart, M., et al., 2019. Impaired endothelial autophagy promotes liver fibrosis by aggravating the oxidative stress response during acute liver injury. J. Hepatol. 70, 458–469. https://doi.org/10.1016/j.jhep.2018.10.015.

Saka, W.A., , 2024. L-arginine attenuates dichlorvos-induced testicular toxicity in male Wistar rats by suppressing oxidative stress-dependent activation of caspase 3-mediated apoptosis. Biomedicine & pharmacotherapy = Biomedecine & pharmacotherapie 178, 117136, doi:10.1016/j.biopha.2024.117136 (2024)..

Saka, W.A., Akhigbe, R.E., Abidoye, A.O., Dare, O.S., Adekunle, A.O., 2021. Suppression of uric acid generation and blockade of glutathione dysregulation by L-arginine ameliorates dichlorvos-induced oxidative hepatorenal damage in rats. Biomedicine & pharmacotherapy = Biomedecine & pharmacotherapie 138, 111443, doi: 10.1016/j.biopha.2021.111443 (2021)..

Saravanakumar, K., et al., 2024. Cellular metabolism and health impacts of dichlorvos: occurrence, detection, prevention, and remedial strategies-a review. Environ. Res. 242, 117600. https://doi.org/10.1016/j.envres.2023.117600.

Schmitt, F., Babylon, L., Dieter, F., Eckert, G.P., 2021. Effects of pesticides on longevity and bioenergetics in invertebrates-the impact of polyphenolic metabolites. Int. J. Mol. Sci. 22. https://doi.org/10.3390/ijms222413478.

Shao, Q., et al., 2021. JieZe-1 alleviates HSV-2 infection-induced genital herpes in Balb/c mice by inhibiting cell apoptosis via inducing autophagy. Front. Pharmacol. 12, 775521. https://doi.org/10.3389/fphar.2021.775521.

Singh, S.B., et al., 2010. Human IRGM regulates autophagy and cell-autonomous immunity functions through mitochondria. Nat. Cell Biol. 12, 1154–1165. https://doi.org/10.1038/ncb2119.

Somiael, M., Madiha, F., 2012. Pathological effects of dichlorvos and fenitrothion in mice. Pathol., Res. Pract. 208, 286–291. https://doi.org/10.1016/j.prp.2012.01.010.

Sun, M., et al., 2021. p53 deacetylation alleviates sepsis-induced acute kidney injury by promoting autophagy. Front. Immunol. 12, 685523. https://doi.org/10.3389/fimmu.2021.685523.

Sun, P., et al., 2022. Application of three prediction models in pesticide poisoning. Environ. Sci. Pollut. Res. Int. 29, 30584–30593. https://doi.org/10.1007/s11356-021-17957-7.

Tang, Z., et al., 2021. HO-1-mediated ferroptosis as a target for protection against retinal pigment epithelium degeneration. Redox Biol. 43, 101971. https://doi.org/10.1016/j.redox.2021.101971.

Trivedi, S.P., Ratn, A., Awasthi, Y., Kumar, M., Trivedi, A., 2021. In vivo assessment of dichlorvos induced histological and biochemical impairments coupled with expression of p53 responsive apoptotic genes in the liver and kidney of fish, Channa punctatus (Bloch, 1793). Comp. Biochem. Physiol. Toxicol. Pharmacol.: CBP 245, 109032. https://doi.org/10.1016/j.cbpc.2021.109032.

Wang, L.Y., Fan, R.F., Yang, D.B., Zhang, D., Wang, L., 2019. Puerarin reverses cadmium-induced lysosomal dysfunction in primary rat proximal tubular cells via inhibiting Nrf2 pathway. Biochem. Pharmacol. 162, 132–141. https://doi.org/10.1016/j.bcp.2018.10.016.

Xu, T., et al., 2018. Neferine, is not inducer but blocker for macroautophagic flux targeting on lysosome malfunction. Biochem. Biophys. Res. Commun. 495, 1516–1521. https://doi.org/10.1016/j.bbrc.2017.11.169.
Xu, Y., Li, Y., Li, J., Chen, W., 2022. Ethyl carbamate triggers ferroptosis in liver through inhibiting GSH synthesis and suppressing Nrf2 activation. Redox Biol. 53, 102349. https://doi.org/10.1016/j.redox.2022.102349.
Yang, L., et al., 2022. Lactobacillusjohnsonii L531 protects against salmonella infantis-induced intestinal damage by regulating the NOD activation, endoplasmic reticulum stress, and autophagy. Int. J. Mol. Sci. 23. https://doi.org/10.3390/ijms231810395.
Zhang, Q., Cao, S., Qiu, F., Kang, N., 2022. Incomplete autophagy: trouble is a friend. Med. Res. Rev. 42, 1545–1587. https://doi.org/10.1002/med.21884.
Zhang, X., et al., 2024. IRGM/Irgm1 increases autophagy to inhibit activation of NLRP3 inflammasome in inflammatory injury induced acute liver failure. Cell Death Discov. 10, 272. https://doi.org/10.1038/s41420-024-02052-w.